Predicting Target Displacements Using Ultrasound Elastography and Finite Element Modeling

Jorn op den Buijs, Hendrik H. G. Hansen, *Student Member, IEEE*, Richard G. P. Lopata, *Member, IEEE*, Chris L. de Korte, *Member, IEEE*, and Sarthak Misra*, *Member, IEEE*

***Abstract*—Soft tissue displacements during minimally invasive surgical procedures may cause target motion and subsequent misplacement of the surgical tool. A technique is presented to predict target displacements using a combination of ultrasound elastography and finite element (FE) modeling. A cubic gelatin/agar phantom with stiff targets was manufactured to obtain pre- and post-loading ultrasound radio frequency (RF) data from a linear array transducer. The RF data were used to compute displacement and strain images, from which the distribution of elasticity was reconstructed using an inverse FE-based approach. The FE model was subsequently used to predict target displacements upon application of different boundary and loading conditions to the phantom. The influence of geometry was investigated by application of the technique to a breast-shaped phantom. The distribution of elasticity in the phantoms as determined from the strain distribution agreed well with results from mechanical testing. Upon application of different boundary and loading conditions to the cubic phantom, the FE model-predicted target motion were consistent with ultrasound measurements. The FE-based approach could also accurately predict the displacement of the target upon compression and indentation of the breast-shaped phantom. This study provides experimental evidence that organ geometry and boundary conditions surrounding the organ are important factors influencing target motion. In future work, the technique presented in this paper could be used for preoperative planning of minimally invasive surgical interventions.**

***Index Terms*—Computer-assisted surgery, elastography, finite element analysis, minimally invasive surgery, preoperative planning, strain, ultrasound.**

I. Introduction

DURING many minimally invasive surgical interventions, such as fine needle aspiration, core biopsy, interstitial brachytherapy or radiofrequency ablation, the clinician inserts a surgical tool into the body with the intention to reach a specific target, e.g., a suspected malignant lesion [1], [2]. Such interventions are generally performed using ultrasound or other imaging modalities to assist the clinician in targeting the lesion [3]–[5]. Breast biopsy is an example of a procedure that requires target-specific surgical tool insertion (Fig. 1). For precise diagnosis and/or therapy, accurate surgical tool placement is of utmost importance [6], especially since the detected targets are getting smaller with increased diagnostic performance. However, organ deformation due to patient motion, physiological processes, and tool-tissue interactions may result in motion of the target [7], preventing the surgical tool from reaching its intended target. Thus, several interventional radiology procedures would benefit from a patient-specific preoperative plan for drug delivery and biopsies. Such plans would predict the target motion and thereby improve the clinical outcome of the procedure.

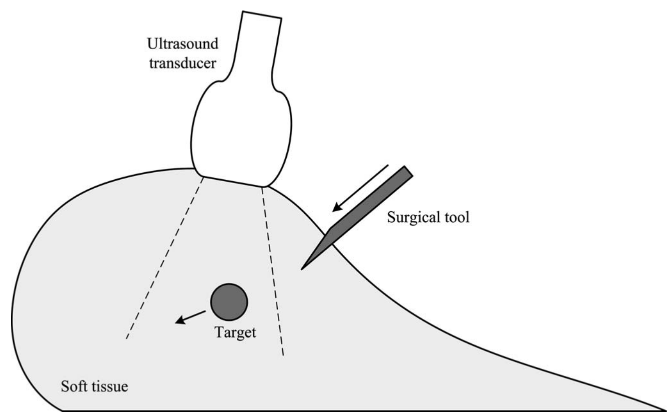

Fig. 1. Schematic of an ultrasound-guided minimally invasive surgical intervention in breast tissue: Compression by the ultrasound transducer, as well as interactions between surgical tool and soft-tissue cause target motion.

Accurate computer-based simulation of tissue and target deformation upon medical interventions could aid surgeons in training and preoperative planning of complex procedures. For example, finite element (FE) modeling could be used to predict bladder deformation for improvement of image-guided radiotherapy [8], or to predict breast deformation upon craniocaudal and mediolateral oblique compression [9]. In addition, computer models of surgical procedures may be used for development of novel medical devices, or serve as input for controllers of robotic surgical systems [10], [11]. Simulations of surgical tool trajectories and target motion require the development of realistic, patient-specific biomechanical modeling of tissues and their interactions with the surrounding organs, as well as the instrumentation tools [12]. However, developing

Manuscript received March 14, 2011; revised June 17, 2011; accepted August 3, 2011. Date of publication August 15, 2011; date of current version October 19, 2011. This work was supported by grants from the Netherlands Organization for Scientific Research (NWO). *Asteriks indicates corresponding author.*

J. op den Buijs is with MIRA — Institute of Biomedical Technology and Technical Medicine (Control Engineering Group), University of Twente, The Netherlands.

H. H. G. Hansen and C. L. de Korte are with the Department of Pediatrics (Clinical Physics Laboratory), Radboud University Nijmegen Medical Centre, The Netherlands.

R. G. P. Lopata is affiliated with the Department of Biomedical Engineering (Cardiovascular Biomechanics Group), Eindhoven University of Technology, The Netherlands.

*S. Misra is with MIRA — Institute of Biomedical Technology and Technical Medicine (Control Engineering Group), University of Twente, The Netherlands (e-mail: s.misra@utwente.nl).

Color versions of one or more of the figures in this paper are available online at http://ieeexplore.ieee.org.

Digital Object Identifier 10.1109/TBME.2011.2164917

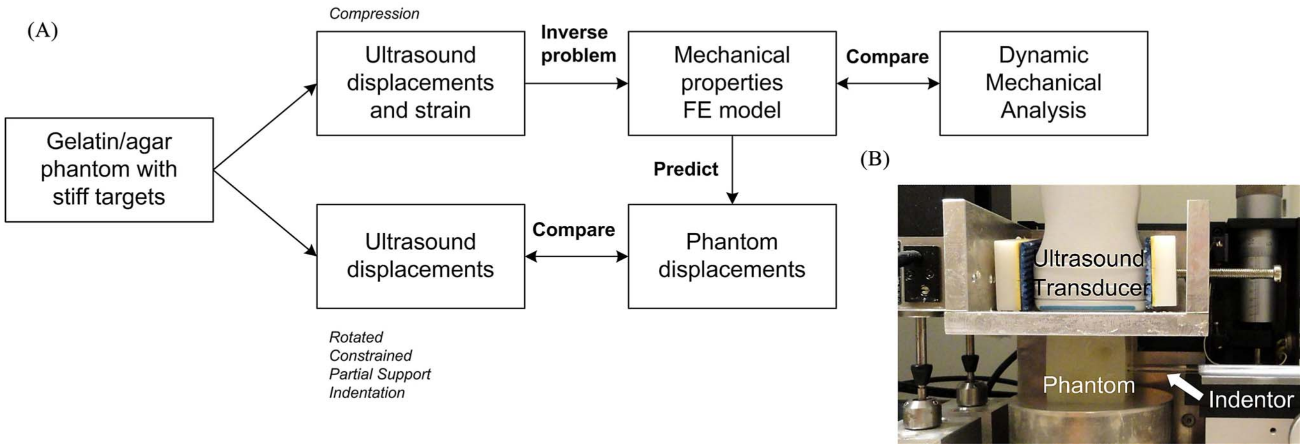

Fig. 2. (A) Overview of the cubic phantom study: A gelatin/agar phantom was fabricated to measure strains and displacements during the case *Compression*. Elastic properties for a finite element (FE) model were obtained by solving an inverse problem. This FE model was then used to predict the displacements for the other cases (*Rotated*, *Constrained*, *Partial Support*, *Indentation*). Model predictions were then compared to experimental data. (B) Picture of the experimental setup. The phantom is placed between the two platens of a compression setup. An ultrasound transducer is mounted to the top platen. An indentor on a linear translation stage is used to indent the phantom with a cylindrical rod.

accurate biomechanics-based models for surgical simulation is challenging. Biological tissues are generally inhomogeneous, anisotropic, and viscoelastic. Further, development of organ models requires measurement of tissue properties *in vivo*, since organs have significantly different dynamics, which are impossible to precisely replicate during *ex vivo* experiments. On the other hand, using current medical imaging modalities such as X-ray, ultrasound, computed tomography (CT) scans, and magnetic resonance (MR) images, it is possible to determine organ geometry with a high level of accuracy. Complex boundary constraints and connective tissues that support the organs can also be observed, but to a lesser degree. In a previous study, it was shown by means of numerical models of tissue displacements that organ geometry and boundary constraints dominate target motion [13]. Changes in boundary conditions could be caused by patient motion, or the presence or absence of surrounding anatomical constraints, such as boney structures or connective tissue. Variations in loading conditions could be due to compressive displacements by the ultrasound transducer, or indentation by needles or other surgical tools. Noninvasive predictions of target motion under altered conditions would be valuable for preoperative planning of surgical tool trajectories in ultrasound-guided minimally invasive surgery.

The goal of this study was to confirm that a linear finite element (FE) model based on ultrasound-measured elastic properties can predict target displacements under various loading and boundary conditions. Finite element methods are suitable techniques for models of soft tissue deformation [14]. A previous study used various FE models to predict breast tissue displacement after compression [15], and several recent studies have attempted to model insertion of needles into soft tissue [16]–[18]. FE models to predict motion of inhomogeneous tissues require an estimation of the tissue stiffness. A noninvasive *in vivo* technique for estimation of the spatial variation of mechanical properties is ultrasound elastography. Ultrasound elastography measures tissue deformation and strain [19]–[21], from which the relative distribution of elasticity can be deduced by solving an inverse problem [22], [23]. This technique is mainly being investigated as a diagnostic tool for the detection of targets, such as tumors, since these are generally stiffer than the surrounding tissue [24]. FE modeling and ultrasound elastography are both established techniques. The novel aspect of this study is to show that elastographically estimated tissue elastic modulus distributions can be used in combination with FE models for accurate target displacement predictions upon changes in loading and boundary conditions.

II. Materials and Methods

Experiments were performed using a cubic phantom and a breast-shaped phantom. The overview of the cubic phantom study is shown in Fig. 2(A). A cubic gelatin/agar phantom with two stiff targets was created (Section II-A). We used two stiff targets, since a single target would result in a symmetric strain field. A phantom with two targets results in a more realistic strain field. The phantom was loaded in different conditions and ultrasound images were acquired (Section II-B). Displacement and strain images were obtained from the ultrasound measurements using a cross-correlation algorithm (Section II-C). An inverse problem was then solved to obtain the distribution of elastic moduli from the strain images (Section II-D), which were verified using mechanical tests on the phantom materials (Section II-F). We used the distribution of elastic modulus in an FE model to predict the displacements upon application of different loading and boundary conditions, which are known to be important factors in displacement predictions [13]. The target displacement predictions were verified experimentally with the ultrasound measurements. To investigate the influence of geometry, we used a combination of ultrasound elastography and FE analysis to predict the displacement of a stiff target embedded in the breast phantom upon compression of the phantom by the ultrasound transducer and upon indentation of the phantom (Section II-G).

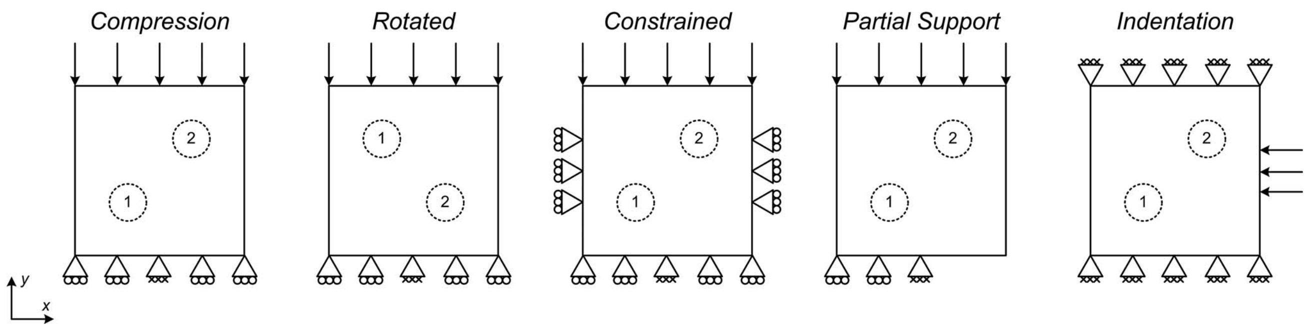

Fig. 3. Schematic of the boundary and loading conditions used in the different cases. Numbers 1 and 2 denote target locations. Arrows indicate the x- and y-directions. Case *Compression* was used as baseline, while other cases are representative of changes in boundary and loading conditions.

A. Preparation of Cubic Phantom for Ultrasound Measurements

A cubic tissue phantom was made using two solutions of gelatin (Dr. Oetker, Ede, The Netherlands), agar (Boom, Meppel, The Netherlands), and silica gel (particle size $< 63\,\mu$ SiC, E. Merck, Darmstadt, Germany) in water. The agar concentration was different for each gel to control the stiffness, whereas tissue acoustic scattering was mimicked by the silica gel. Solutions for the soft surrounding material and stiff targets were prepared at the same time. The surrounding material was made from a solution of 8.0%-by-weight gelatin, 1.0%-by-weight agar, and 1.0%-by-weight silica gel in water, which was obtained by adding the gelatin, agar, and silica gel to boiling water. The mixture was boiled until the particles were dissolved. The solution was then poured into a cubic acrylic mold ($40 \times 40 \times 40$ mm^3). Two plastic cylinders with diameter of 8 mm were placed in the cubic mold, as placeholders for the targets. The gel for the targets was made from a solution of 8.0%-by-weight gelatin, 3.0%-by-weight agar, and 1.0%-by-weight silica gel in water. After solidification of the surrounding material for about 1 h at 7 °C, the plastic cylinders were removed, and the resulting cylindrical holes were filled with the stiffer gel. The mixture was then allowed to solidify at 7 °C and the phantom was carefully removed from the mold. The phantom was allowed to solidify at approximately 7 °C for four days before experimental testing, to reach stable elastic moduli for the surrounding material and targets [25].

B. Ultrasound Experiments

The gelatin/agar phantom was placed between the rigid platens of a compression setup (Fig. 2B), of which the top platen could be translated vertically using a manual micrometer. The linear array transducer of the ultrasound system was anchored in the center of the top platen. Radio-frequency (RF) ultrasound data were recorded with a SONOS 7500 real-time 3D system (Philips Medical Systems, Best, The Netherlands), equipped with a linear array transducer (L11-3) with a central frequency of 7.5 MHz.

RF data were sampled at 39 MHz and were acquired in the unstressed state, and after applying each of the following five cases to the cubic gelatin/agar phantom (Fig. 3):

1) *Compression*: Compressive axial displacements in five steps of 1.2 mm (3% strain for a cube of height 40 mm) were applied to the top face of the phantom. Hence, a total displacement of 6.0 mm (15% strain) was applied. The displacements were applied in increments because the RF-based strain algorithm has been shown to correctly estimate the strains and displacements for strains up to 5% for the window size used [26].
2) *Rotated*: Identical loading as for *Compression*; however, the specimen was rotated 90° clockwise.
3) *Constrained*: Identical loading as for *Compression*. The side faces of the specimen were partially constrained in the lateral direction by using a 14 mm wide clamp.
4) *Partial Support*: Identical loading as for *Compression*; however, only half of the bottom face of the specimen was supported by the bottom platen of the compression setup.
5) *Indentation*: The specimen was indented in two steps of 0.5 mm to a total indentation of 1.0 mm from the right side with an indentor of 4.0 mm diameter, mounted on a linear stage with manual micrometer. The phantom was gently clamped between the top and bottom platens to ensure indentation did not result in horizontal sliding of the phantom.

The case *Compression* was used as a baseline, i.e., this case was used to estimate the relative distribution of mechanical properties in the phantom. The other cases were used to simulate changes in boundary and loading conditions.

C. Displacement and Strain Estimation

A previously published method was used to estimate displacements and strains [21]. In brief, a coarse-to-fine displacement estimation algorithm was used to calculate axial (y-direction) and lateral (x-direction) displacements. Two-dimensional (2D) windows of RF data were cross-correlated and the resulting peak of the cross-correlation function was detected using 2D parabolic interpolation to achieve subsample resolution. The algorithm used the RF signal envelope at coarse scale during the first iteration, and full RF data for all subsequent iterations. Four iterations with pre-compression window lengths of 200, 100, 50, and 25 samples were performed for coarse-to-fine displacement estimation. Two additional iterations (window length of 25 samples) with aligning and stretching of the post-compression data were performed. The size of the pre-compression window

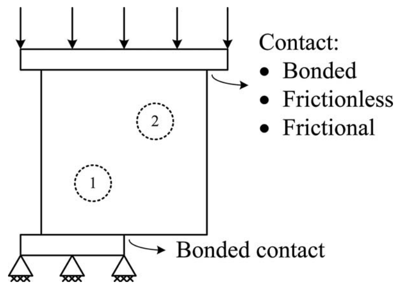

Fig. 4. Contact boundary conditions for case *Partial Support*. The contact between top loading platen and phantom was varied between bonded, frictionless, and frictional contact.

size in lateral direction was 11 samples. During each iteration, the post-compression window was two times larger than the pre-compression window in the axial direction, and the axial window overlap was set to 50%. The window overlap was 89% in the lateral direction. Sub-step displacements were tracked in order to calculate large displacements. Since the phantoms were made of water-based solutions of gelatin and agar, we assumed the speed of sound of water (1540 m s^{-1}) in the displacement calculations. Axial strains were calculated using a least-squares strain estimator. Calculations were performed in MATLAB (The Mathworks Inc., Natick, USA). For visualization purposes, B-mode images were obtained by taking the 10-base logarithm of the absolute value of the Hilbert transform of the RF data.

D. Finite Element Model

The FE method was used in the reconstruction of elastic moduli and subsequent prediction of displacements under different loading and boundary conditions. A 2D plane-stress analysis was performed. In the absence of body forces, the equilibrium equation is given by

$$\nabla \cdot \boldsymbol{\sigma} = 0 \tag{1}$$

where $\boldsymbol{\sigma}$ is the stress tensor. Assuming linear elastic and isotropic material properties within the element, the constitutive equation is given by

$$\boldsymbol{\sigma} = \frac{E}{1+\nu}\varepsilon + \frac{E\nu}{(1+\nu)(1-2\nu)}\mathrm{tr}(\varepsilon)\mathbf{I} \tag{2}$$

with ε the strain tensor, tr the trace operator, $\mathbf{I}$ the second-order identity tensor, E the Young's modulus, and ν the Poisson's ratio. The Young's modulus was allowed to vary among elements. The Poisson's ratio was assumed to be spatially invariant and equal to 0.495 under the assumption of a nearly incompressible material.

Strains were related to the displacements via the Green-Lagrange strain tensor

$$\varepsilon = \frac{1}{2}\left[\nabla\mathbf{u} + (\nabla\mathbf{u})^T + (\nabla\mathbf{u})^T\nabla\mathbf{u}\right] \tag{3}$$

where $\mathbf{u}$ are the displacements.

To reconstruct the relative mechanical properties from the axial strains, the plane-stress variant of an iterative method [27] was used. Since we did not measure the pressure exerted by the ultrasound transducer, the absolute value of the Young's modulus was not estimated by the algorithm, and therefore it was only possible to obtain the ratio between the Young's moduli of the stiff targets and the surrounding material. The algorithm was initialized with a homogeneous distribution of the relative Young's modulus $E = 1$ at iteration $k = 0$ to obtain an initial prediction of stresses and strains. The Young's moduli were then adapted according to

$$E^{k+1} = \frac{\sigma_y^k - \nu\sigma_x^k}{\varepsilon_y^{\mathrm{data}}} \tag{4}$$

where σ_x and σ_y are the lateral and axial stress components, respectively. These stress components were obtained from the forward FE problem. It should be noted that calculated stresses and pressures in the computations did not have absolute values, but their ratios were still meaningful. The axial strain ε_y^{data} was obtained from the ultrasound strain image under the case *Compression*.

Due to windowing in the displacement-tracking algorithm, artifacts may arise at the image boundaries. Additionally, pixels at the image boundaries may move out of the field of view during mechanical compression of the phantom. Therefore, we chose to focus on a smaller region of interest than the full image. The strains were only measured inside a 28×28 mm^2 region of interest, and the relative Young's modulus was kept constant at $E = 1$ for the elements outside the region of interest. The stresses were obtained by solving a plane-stress FE model with 160×160 linear quadrilateral elements with element edge length of 0.25 mm. Mesh resolution studies were performed to confirm that the computed displacements were independent from element size at this resolution. Convergence of the Young's modulus distribution was reached after ten iterations. The estimated distribution of relative elastic moduli from the case *Compression* was subsequently used to predict the target displacements of the cases with the varying boundary and loading conditions, i.e, cases *Rotated*, *Constrained*, *Partial Support*, and *Indentation* (Section II-B).

The FE calculations were performed with Tool Command Language (Tcl) scripts invoked from the commercial software ANSYS Mechanical (ANSYS Inc., Canonsburgh, USA). Computations were executed on an eight-core 64-bit Intel Xeon workstation with 12 GByte internal memory running Microsoft Windows 7 Professional.

E. Contact Boundary Conditions

Initially, the boundary conditions were modeled as displacement loads applied directly to the boundary nodes of the FE mesh. For the case *Partial Support*; however, there is a strong effect of friction between the phantom and the top compression platen. Therefore, we incorporated the contact of the phantom with loading platens into the FE model. We took three types of contact into consideration: bonded contact, frictionless contact, and frictional contact. Bonded contact meant that the surfaces of the contacting objects were assumed to be sticking and, hence, could not slide relative to each other. Frictionless contact allowed for free sliding at the contact interface. During frictional

Fig. 5. Breast phantom: The mold was designed using computer-aided design software and printed using a 3-D printer. The figure shows the gel after solidification and removal from the mold.

contact, the contact depended on the equivalent shear stress carried by the contacting interfaces. If the shear stress at the contact surface was less than a certain limiting value, the contacting surfaces were assumed to be sticking. If the shear stress exceeded the limiting value, the surfaces were assumed to be sliding. The limiting shear stress $\tau_{\rm lim}$ was computed as

$$\tau_{\rm lim} = \mu P \tag{5}$$

where μ is the coefficient of friction and P is the contact normal pressure. It should be noted that we did not measure absolute values for the stresses and pressures; however, the ratios of the stresses and pressures are still valid. In (5), the limiting shear stress is compared with contact pressure. This ratio has no units, and therefore the actual absolute values of the stresses are not required.

For the case *Partial Support*, contact with the bottom loading platen was modeled as bonded contact, whereas contact between the top loading platen and the phantom was varied between bonded, frictionless, and frictional (Fig. 4). Furthermore, for the breast phantom studies (Section II-G), contact of the breast phantom surface with the ultrasound transducer or the indentor was also modeled as frictional contact. In these cases, the contact interface area changes upon compression due to the curved surface of the breast phantom. For all cases with frictional contact, the value for the frictional coefficient in (5) was assumed $\mu = 0.1$. This value was chosen to be lower than a previously reported frictional coefficient for a soft tissue phantom [28], because in our case the phantom surface was lubricated with gel.

F. Dynamic Mechanical Testing

Dynamic mechanical tests on the phantom gels were performed to verify the results of the relative Young's modulus reconstruction based on the ultrasound strain images. Layers of 3.5 mm were poured using the same batches of the agar/gelatin solutions as used during phantom preparation. After solidification for four days at approximately 7 °C, three circular specimens (diameter of 25 mm) were punched from the layers for both the 1% and 3% agar gels. The specimens were carefully placed between the loading platens of a rheometer (Anton Paar, Gentbrugge, Belgium). A normal force of 5 N was applied to the specimens to ensure they were clamped between the two platens. A sinusoidal radial shear strain with amplitude of 1% was applied to the specimens. The frequency of the sinusoidal shear strain was 0.1 Hz. The rheometer measured the resulting torque and phase lag to determine the storage and loss moduli G' and G'', respectively. The shear modulus G was assumed $G = G'$. Also, for homogeneous isotropic materials the Young's modulus $E = 2G(1 + \nu)$.

G. Application to Breast-Shaped Phantom

To investigate whether the combination of elastography and FE analysis could be applied to a more clinically relevant scenario of organ-shaped geometries, we manufactured a phantom in the shape of a breast with a stiff target to mimic a tumor. The phantom was also prepared using gelatin/agar solutions with concentrations of gelatin, agar, and silica gel for the surrounding material and the stiff target that were identical to that for the cubic phantom (Section II-A). A breast-shaped mold ($14 \times 10 \times 6$ cm^3) was designed using SolidWorks 3-D computer-aided design (CAD) software (Dassault Systèmes SolidWorks Corp., Concord, USA), converted to a stereolithography (STL) file format, and printed using an Objet Eden250 3-D printer (Objet Geometries Inc., Billerica, USA). After filling half the mold with the solution for the surrounding material, it was allowed to solidify for about 1 h at 7 °C. To mimic a tumor, a semi-spherical hole with diameter of approximately 10 mm was carefully cut into the gel. This hole was filled with the stiffer gel and allowed to solidify, such that the stiffer material formed a protuberance at the surface. The thought behind this was to include a stiff target in the phantom which was somewhat spherical in shape, although a perfect sphere could not be achieved. The inclusion was placed in the middle to minimize out-of-plane motion. Thereafter, the mold was completely filled with gel for the surrounding material. After solidification, the phantom was carefully removed from the mold (Fig. 5).

Three experiments were carried out with the breast phantom. The first experiment aimed to reconstruct the distribution of elastic properties in a plane intersecting the stiff target embedded in the phantom. For this purpose, the ultrasound transducer was manually pressed against the phantom, such that it made contact with the transducer surface and slight pre-compression strain was applied. During a period of approximately 3 s, the transducer was then used to compress the phantom more and return to its initial position. RF data were recorded at 25 Hz during this period. The images were analyzed with the 2D strain algorithm [21] to compute incremental displacements between frames. The total deformation and strain were calculated from these sub-step displacements. A 2D plane-stress FE model and (4) were then used to iteratively compute the relative Young's modulus distribution. FE axial displacements at the boundary nodes were set equal to the axial displacements obtained by the ultrasound displacement algorithm (Section II-C).

The aim of the second breast phantom experiment was to predict the motion of the target during a similar compression experiment, as described above. For this case, a 3D FE model was constructed from the CAD drawing used to create the breast phantom mold. The target in the breast phantom was spherical

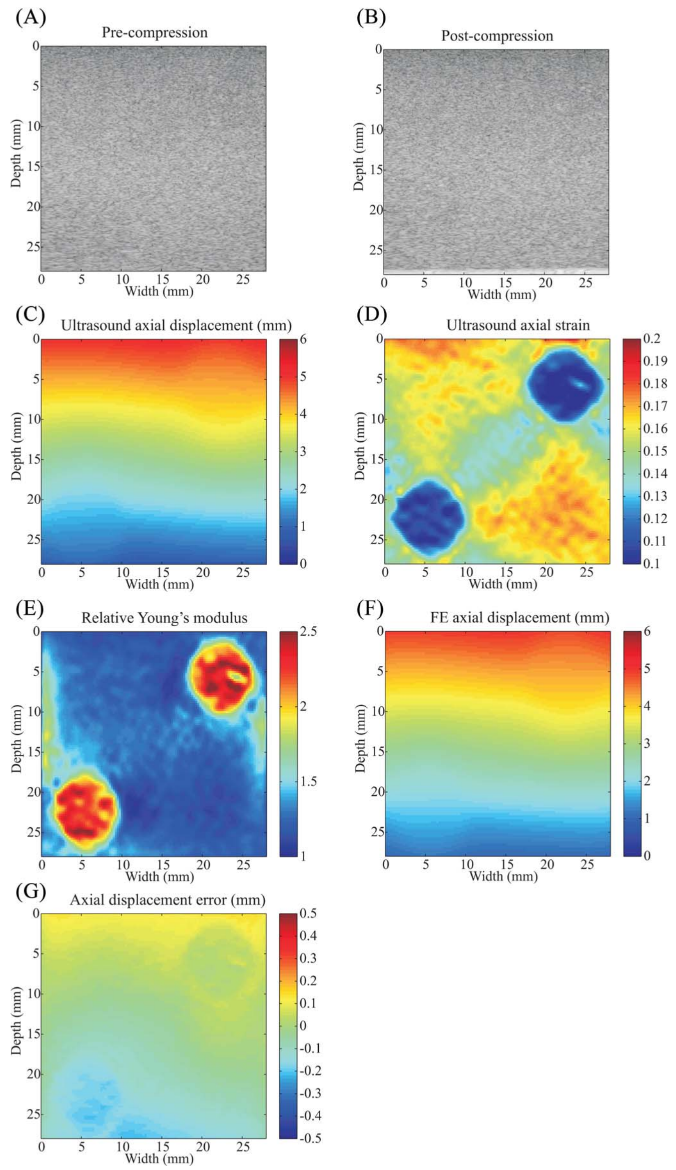

Fig. 6. Ultrasound measurements, displacement and strain estimation, and reconstruction of relative Young's modulus distribution from ultrasound strain images for the case *Compression*. (A) B-mode ultrasound image of the phantom at rest. (B) B-mode ultrasound image after axial compression of the phantom by 6.0 mm. (C) Axial displacements estimated from RF data. (D) Axial strains in the phantom. (E) Reconstructed relative Young's modulus distribution. (F) Finite element-(FE) predicted axial displacements. (G) Error between measured and predicted axial displacements.

in shape and was, therefore, modeled as a 10.0 mm diameter sphere. It should be pointed out that a perfect sphere could not be achieved during the phantom fabrication, and this may have introduced errors in the FE model. The ratio of the Young's modulus of target and surrounding material was set equal to the ratio as measured during the first breast compression experiment. It should be noted that this was also done for the elements outside the plane used for the elastography experiment described above. The ultrasound transducer was also incorporated into the model, to account for the contact between the transducer and the curved surface of the breast phantom. In the model, the ultrasound transducer was initially not in contact with the breast surface. By simulating a displacement of 3.0 mm in the normal direction of the transducer surface, complete contact with the breast surface was established. The modeled ultrasound transducer was then further displaced in the normal direction by the same amount of transducer displacement as measured in the ultrasound experiment. Contact between the ultrasound transducer and the breast surface was modeled as frictional contact with $\mu = 0.1$, as described by (5) in Section II-E. The displacement of the target as a result of the compression by the ultrasound transducer was computed from the FE simulation, and compared to the target displacement as measured by ultrasound. During the experiment, the ultrasound transducer was placed on the symmetry axis of the breast, such that the out-of-plane motion was negligible in the plane visualized by the ultrasound transducer. This allowed comparison of the 3D FE model with the ultrasound-measured displacements.

In the third experiment, an 8.0 mm diameter indentor was used to manually indent the breast surface by approximately 4.0 mm, while the ultrasound transducer was firmly held against the breast surface for imaging purposes. Both the ultrasound transducer and the indentor were included in the 3D FE model, and the contact between the indentor and the breast surface was modeled as frictional contact with $\mu = 0.1$. The total displacement field as predicted by FE simulation from the indentation was compared to ultrasound measurements of the total displacement field, and the error was calculated at the center of the stiff target.

III. Results

We begin by presenting the results for the experiments and FE simulations on the cubic phantom (Section III-A). This is followed by the results for the experiments performed on the breast-shaped phantom (Section III-B).

A. Cubic Phantom

Ultrasound RF data were collected using the cubic phantom with two stiff targets in the case *Compression*. These data were then used to compute displacement and strain images, from which the distribution of elastic moduli in the phantom was reconstructed (Section III-A1). These elastic moduli were then compared with dynamic mechanical tests on small samples of the phantom material (Section III-A2). Thereafter, the estimated mechanical properties were used in the FE model to predict the displacements under the different loading and boundary conditions (Section III-A3).

1) Reconstruction of Elastic Modulus Distribution From Strain Image: B-mode images before and after loading of the specimen in the case *Compression* did not reveal the targets in the phantom, due to the equal amount of ultrasound scattering particles in both gels (Fig. 6A and B). The locations of the target can be perceived from the axial displacement image, obtained by application of the cross-correlation of the pre- and post-compression RF data outlined in Section II-C (Fig. 6C). The axial strain image was obtained by applying a least-squares strain estimator [26], [29] (Fig. 6D). The strain distribution clearly reveals the location of the targets, with the strains in the targets

TABLE I
RATIO OF THE ELASTIC MODULUS (E) FOR THE 1% AND 3% AGAR GELS, AS MEASURED BY DYNAMIC MECHANICAL ANALYSIS (DMA) AND BY ULTRASOUND ELASTOGRAPHY

Method	E 1% agar (kPa)	E 3% agar (kPa)	Ratio
DMA	22.1 ± 3.4	57.7 ± 0.2	2.6
Elastography (target 1)	-	-	2.2 ± 0.1
Elastography (target 2)	-	-	2.3 ± 0.2

lower than in the surrounding material. The inverse problem detailed in Section II-D was then solved and after ten iterations, the relative Young's modulus distribution was converged (Fig. 6E). Relative Young's moduli of the targets were determined by manually defining contours around the targets. Target 1 showed a relative Young's modulus of 2.2 ± 0.1, whereas this value was 2.3 ± 0.2 for target 2 (Table I). This distribution of elastic moduli was subsequently used to predict the axial displacements by the FE method (Fig. 6F), and the axial displacement errors were obtained by subtracting the FE-predicted displacements from the displacements measured by ultrasound (Fig. 6G). The axial displacement errors in the region of interest ranged from -0.21 to 0.15 mm.

2) Comparison With Dynamic Mechanical Tests: Dynamic mechanical analysis (DMA) of the prepared gels were carried out at room temperature to determine the storage and loss moduli at a frequency of 0.1 Hz (Table I). The elastic modulus was then calculated as described in Section II-F. The variance in the Young's modulus of the surrounding material was higher than that of the target material. Most likely, this was due to the fact that the samples of lower stiffness contain more water and are, therefore, more likely to dry out during the DMA measurements. According to the DMA tests, the 3% agar gels were 2.6 times stiffer than the 1% agar gels. This is higher than the estimation of the relative Young's modulus by ultrasound elastography. This difference could be explained by the lower relative elastic modulus values determined at the boundaries of the targets in the elastography method. If the elasticity contrast was increased to 2.6 (the value we found with DMA), the total displacement of target 1 decreased by 0.4% from 1.91 mm to 1.90 mm and the total displacement of target 2 remained unchanged at 4.35 mm. If a homogeneous elasticity distribution was used, the total displacement of target 1 increased by 6.4% to 2.03 mm and the total displacement of target 2 decreased by 1% to 4.31 mm. Thus, including the relative elastography distribution in the simulations helped to reduce the prediction error.

3) Finite Element Model Validation: Using the FE model with reconstructed elastic moduli from the case *Compression*, target displacements were predicted for the cases *Rotated*, *Constrained*, *Partial Support*, and *Indentation*, which represent changes in boundary and loading conditions. The predicted target displacements were compared to the corresponding ultrasound measurements after manually aligning the ultrasound-based displacement images to the FE model, using the targets as markers (Fig. 7). In a qualitative sense, it can be noted that FE-predicted displacement fields followed similar trends as the ultrasound-measured displacements. This became particularly clear in the cases *Partial Support* and *Indentation*, where the displacement field showed a distinct pattern as compared to the other boundary and loading conditions. The FE-predicted lateral and axial displacement values at the center of the two targets were obtained for all loading and boundary conditions, and compared to the ultrasound displacement measurements (Table II).

TABLE II
COMPARISON OF AXIAL, LATERAL, AND TOTAL DISPLACEMENTS FOR THE DIFFERENT CASES: FINITE ELEMENT (FE) AND ULTRASOUND (US)

Target 1		*Compression*	*Rotated*	*Constrained*	*Partial Support*	*Indentation*
Axial	US	1.59 mm	4.30 mm	1.57 mm	1.65 mm	0.00 mm
	FE	1.76 mm	4.29 mm	1.92 mm	1.69 mm	0.01 mm
Lateral	US	1.07 mm	0.87 mm	1.03 mm	0.76 mm	0.10 mm
	FE	0.75 mm	0.80 mm	0.39 mm	1.61 mm	0.19 mm
Total	US	1.92 mm	4.39 mm	1.87 mm	1.81 mm	0.10 mm
	FE	1.91 mm	4.36 mm	1.96 mm	2.34 mm	0.19 mm
	Error	0.01 mm 0%	0.03 mm 1%	0.09 mm 5%	0.53 mm 29%	0.08 mm 82%
Target 2		*Compression*	*Rotated*	*Constrained*	*Partial Support*	*Indentation*
Axial	US	4.33 mm	1.57 mm	4.24 mm	4.92 mm	0.07 mm
	FE	4.29 mm	1.66 mm	4.12 mm	5.68 mm	0.04 mm
Lateral	US	0.60 mm	0.67 mm	0.30 mm	2.98 mm	0.21 mm
	FE	0.72 mm	0.67 mm	0.39 mm	4.93 mm	0.26 mm
Total	US	4.37 mm	1.71 mm	4.26 mm	5.75 mm	0.22 mm
	FE	4.35 mm	1.79 mm	4.14 mm	7.52 mm	0.26 mm
	Error	0.02 mm 1%	0.08 mm 5%	0.12 mm 3%	1.77 mm 31%	0.04 mm 19%

Errors were reported as absolute distance (in mm) and as percentage of the ultrasound-measured displacement.

Quantitatively, the total displacement predictions by the FE model resulted in small absolute errors with the validation measurements for the cases *Compression*, *Rotated*, *Constrained*, and *Indentation*. The maximum errors were 0.08 mm for target 1 and 0.11 mm for target 2, for the *Constrained* case. To calculate these errors, we subtracted the FE-predicted displacement image from the displacement image measured with ultrasound. Therefore, these errors can be attributed in part to registration errors between ultrasound image and FE predictions. Noise in the image data could have contributed as well, considering the resolution of the RF data, which is 0.135 mm in the lateral direction and 0.02 mm in the axial direction. For the case *Partial Support*, the difference between total displacement as measured by ultrasound and as predicted by the FE model was large, 0.52 mm for target 1 and 1.77 mm for target 2.

This difference may be attributed to oversimplified modeling of the boundary conditions at the interface of the phantom and the top loading platen. Even though we applied lubrication in the experiment to allow for sliding, the normal forces due to contact at this interface may have induced frictional sliding between phantom and loading platen. This could have caused the lower measured displacements compared to the FE predictions. Furthermore, for the cases *Compression* and *Constrained*, errors in the axial and lateral directions seemed to counterbalance each other, such that the magnitude of the total displacement was well estimated by the FE model, but the direction was not. This resulted in maximum errors in the direction of displacement of 11° for the case *Compression* and 22° for the case *Constrained*. Finally, it was expected that gravity may have played a role for the case *Partial Support*. Therefore, we performed simulation where we included gravity, assuming a density of 1.0 g cm^{-3} for all phantom materials. This resulted in total displacements of the targets that differed less than 1.0% from the displacements for the simulations where gravity was not included.

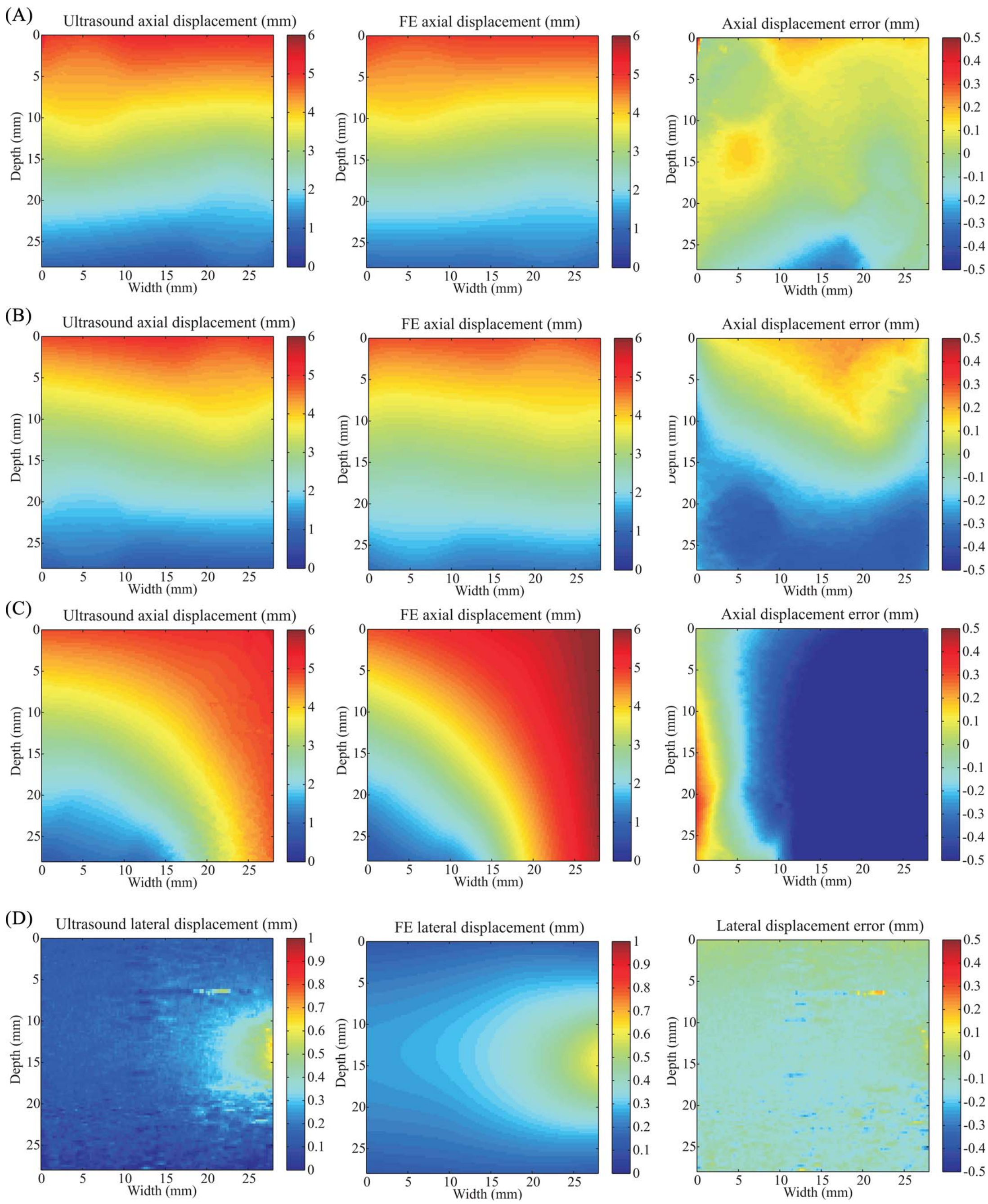

Fig. 7. FE-based predictions of displacements compared to ultrasound measurements during application of different loading and boundary conditions. Axial displacements are compared for the following cases. (A) *Rotated*. (B) *Constrained*. (C) *Partial Support*. Lateral displacements are compared for the following case. (D) *Indentation*.

4) Sensitivity Study — Contact Boundary Conditions: For the case *Partial Support*, large discrepancies between FE-predicted and measured target displacements were found (Section III-A3). We hypothesized that this was due to frictional sliding at the contact interface of the top loading platen and the phantom. Therefore, we studied the sensitivity of the target displacements to boundary conditions for this case. As described in Section II-E, the contact between top loading platen and phantom was varied between bonded, frictionless, and frictional contact. These cases were compared to the ultrasound measurements (Table III). The previous case of applying the boundary conditions directly to the nodes (i.e., no contact) was also incorporated in Table III. This analysis showed that the error in total displacement was reduced to 0.02 mm (1%) for target 1 and 0.34 mm (6%) for target 2 when frictional contact was applied.

B. Breast Phantom

As described in Section II-G, three separate experiments were conducted with the breast phantom. In the first experiment, the

TABLE III
COMPARISON OF AXIAL, LATERAL, AND TOTAL DISPLACEMENTS FOR THE CONTACT CONDITIONS IN THE CASE *PARTIAL SUPPORT*

Target 1	US	No contact	Bonded	Frictionless	Frictional
Axial	1.65 mm	1.69 mm	1.72 mm	1.59 mm	1.67 mm
Lateral	0.76 mm	1.61 mm	0.05 mm	1.75 mm	0.77 mm
Total	1.82 mm	2.33 mm	1.72 mm	2.36 mm	1.84 mm
Error		0.53 mm 29%	0.10 mm 5%	0.54 mm 30%	0.02 mm 1%
Target 2	US	No contact	Bonded	Frictionless	Frictional
Axial	4.92 mm	5.68 mm	5.27 mm	6.00 mm	5.39 mm
Lateral	2.98 mm	4.93 mm	1.00 mm	5.28 mm	2.83 mm
Total	5.75 mm	7.52 mm	5.36 mm	7.99 mm	6.09 mm
Error		1.77 mm 31%	0.39 mm 7%	2.24 mm 39%	0.34 mm 6%

The column with heading Ultrasound (US) contains experimental data. No contact represented applying the boundary condition directly to the nodes (Table II). Errors were reported as absolute distance (in mm) and as percentage of the ultrasound-measured displacement.

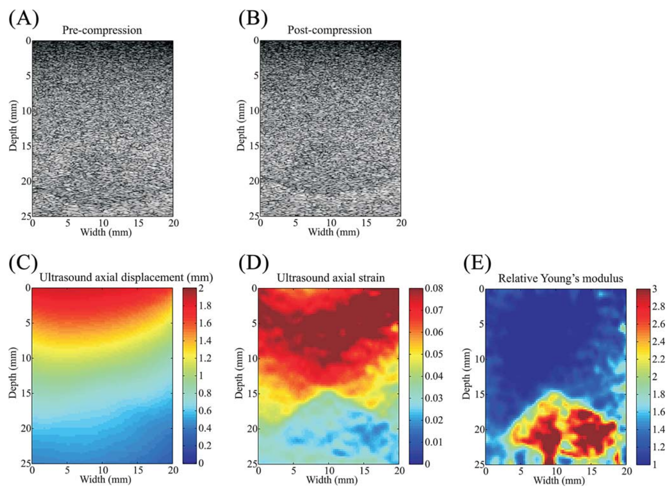

Fig. 8. Reconstruction of relative Young's modulus distribution using the breast phantom. (A) Pre-compression B-mode image of the stiff target inside the breast phantom. The target is visible as the slightly darker spot in the image. (B) Post-compression B-mode image. (C) Axial displacements. (D) Axial strains in the breast phantom. (E) Reconstructed relative Young's modulus.

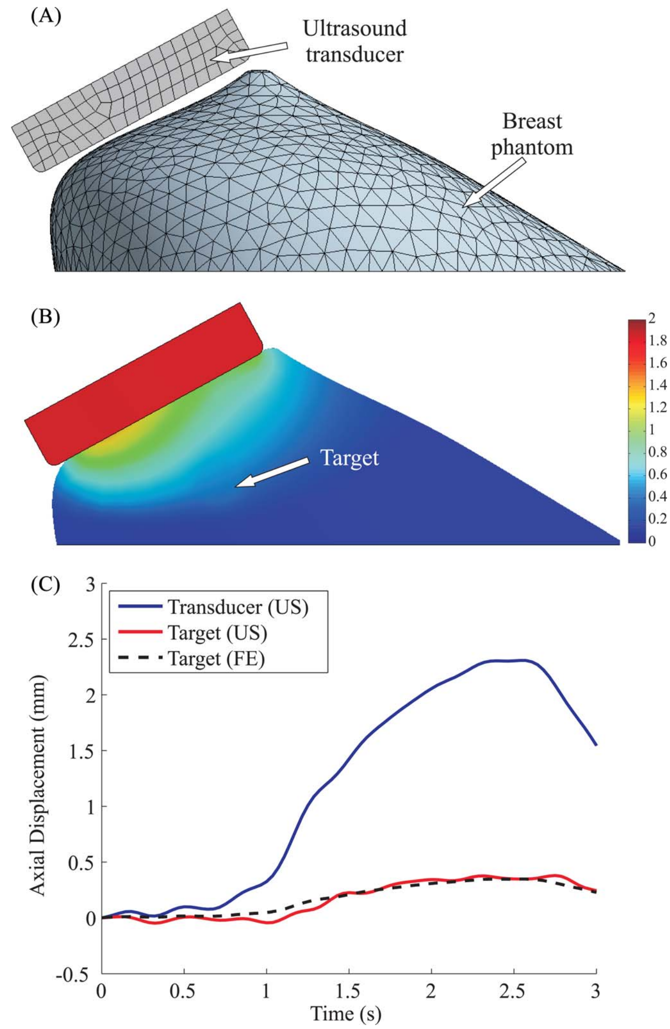

Fig. 9. Prediction of target displacement using the finite element (FE) model. (A) Side view of the FE mesh for the breast phantom and the ultrasound transducer. (B) Section view of the total displacement after compressing the breast phantom with the ultrasound transducer. Displacements are in mm. (C) Ultrasound-measured axial displacements for the ultrasound transducer (blue line) and the target (red line) compared to FE-predicted target displacement (dashed black line).

breast phantom was compressed by the ultrasound transducer, and a series of images were recorded during the compression. The first and final B-mode ultrasound images poorly show the location of the stiff target embedded in the breast phantom (Figs. 8A and B). The axial displacements estimated in the breast phantom (Fig. 8C) clearly show the impact of a complex geometry. Due to the curved surface, the displacements near the surface of the phantom show a semi-circular pattern. In the region of the stiff target, distortions are visible in the axial displacement pattern. The stiff target becomes even more accentuated in the strain image (Fig. 8D), where it can be seen that the strain in the stiffer target is of the order of 2%, about four times lower than the maximum strain at the surface of about 8%. Finally, the stiff target is clearly visible in the reconstructed relative Young's modulus distribution (Fig. 8E). The relative Young's modulus of the target was estimated as 2.5 ± 0.5 by the FE reconstruction algorithm.

The second experiment with the breast phantom was similar to the one described above. The goal of this case was to predict the target displacement due to compression of the breast surface by the ultrasound transducer. A 3D FE model was constructed based on the 3D breast phantom geometry and the mechanical properties from the inversion of the strain distribution. The relative Young's modulus of the inclusion in the FE simulations was set to 2.5 as obtained by the reconstruction of the relative Young's modulus distribution. The ultrasound transducer was also taken into consideration in the model (Fig. 9A). The breast was compressed by the ultrasound transducer along the symmetry axis of the breast, such that out-of-plane motion in the field of view of the ultrasound transducer was negligible. The measured displacement of the ultrasound transducer was used as an input in the FE model, and the model was solved to obtain the displacements in the breast phantom (Fig. 9B). The measured transducer displacement is shown together with the FE-predicted and measured target displacement in Fig. 9C. Peak target displacement was 0.38 mm as measured by

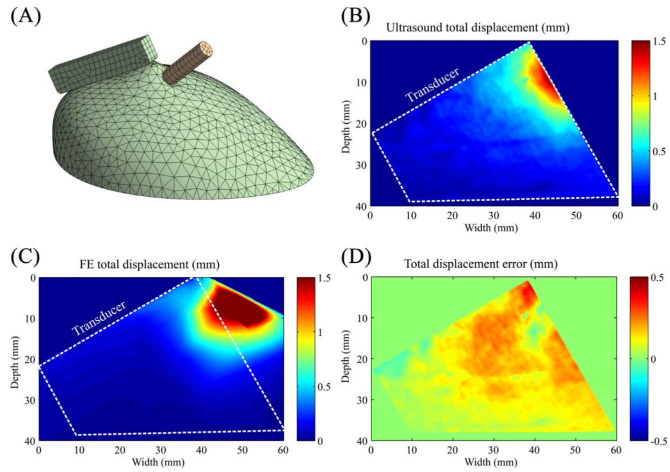

Fig. 10. Prediction of total displacement field using the finite element (FE) model upon indentation of the breast surface. (A) FE mesh for the breast phantom, the ultrasound transducer, and the indentor at the end of the simulation. (B) Total displacement field after indentation as measured by ultrasound. The position of the ultrasound transducer is indicated. (C) Total displacement field after indentation as predicted by the FE model. The field of view of the ultrasound transducer is indicated. (D) Error of the total displacement between ultrasound measurement and FE prediction.

ultrasound and 0.35 mm as predicted by the FE model, resulting in a small error of 0.03 mm (8%).

In the third experiment with the breast phantom, the breast surface was indented by approximately 4.0 mm, while the ultrasound transducer was held against the breast surface. In addition to the ultrasound transducer, the indentor was also taken into consideration in the model (Fig. 10A). The total displacement field as predicted by FE analysis (Fig. 10C) compared well with the total displacement as measured by ultrasound (Fig. 10B). For ease of comparison, the field of view of the ultrasound transducer is indicated in Fig. 10. Quantitative comparison between FE-predicted and measured displacement fields (Fig. 10D) resulted in total displacement errors ranging from -0.21 mm to 0.40 mm (5-10%). This error may in part have resulted from the manual indentation of the breast surface, as this did not allow to accurately incorporate the position, direction, and indentation depth of the indentor into the model.

IV. Discussion and Conclusion

The results presented in this paper demonstrate the feasibility of combining non-invasive strain imaging and FE modeling for predicting displacements of targets during loading and boundary conditions other than the conditions used for strain imaging. Our results indicate that correct modeling of geometry, and loading and boundary conditions, is of utmost importance to achieve accurate target displacement predictions by the FE model.

Ultrasound strain imaging was used to populate the elements of the FE model with relative mechanical properties. The inversion method used to reconstruct relative tissue elasticity from measured axial strains was also based on the FE method [27], and therefore the same FE mesh could be used for inversion and prediction. The mesh did not make any *a priori* assumptions about the geometry of the phantom. Although much research is focused on improvement of the estimation of mechanical properties from ultrasound RF data for diagnostic purposes [30], [31], we showed that the estimated mechanical properties could also be used to predict tissue motion under loading and boundary conditions different than the one used for tissue elasticity reconstruction.

Another novelty of this study was the use of a breast-shaped phantom to conduct strain measurements and reconstruct the relative Young's modulus distribution. Due to the curved surfaces of the phantom, the ultrasound transducer needed to be slightly pressed against the phantom surface to make full contact. Further compression with the ultrasound transducer rendered a strain image in which the target could not be well defined. After reconstructing the relative Young's modulus distribution, the target became visible as a region of higher stiffness. Future work is needed to investigate if solving the inverse problem could aid in increasing the detection of lesions by ultrasound elastography. Furthermore, we used the breast phantom to show that if knowledge about geometry and mechanical properties is available, FE modeling can be used to track target displacements, and to predict displacement fields during compression and indentation of the breast surface. In this study, 3D geometry was obtained from CAD information, but in future clinical studies, geometry should be obtained in 3D with CT scans or MR imaging.

Organ geometry, soft tissue constitutive laws, and boundary conditions imposed by the connective tissue are some of the factors that govern the accuracy during minimally invasive surgery. Preoperative prediction of displacement fields may aid in improving targeting accuracy during minimally invasive procedures, such as needle insertion. Needle insertion procedures are predominantly displacement driven, meaning that the input displacement applied by the clinician results in deformation of the organ. It was recently shown that for such interventions, tissue motion is dominated by the organ's geometry and its boundary constraints [13]. This study corroborates the theoretical predictions of that study, because we found that with *a priori* knowledge of the phantom's geomtery, its loading and boundary constraints, and an estimate of the relative mechanical properties, target motion can be accurately predicted.

A. Directions for Future Work

The ultrasound displacement measurements were performed using a linear array transducer. Therefore, information about the out-of-plane displacements was not available. As a consequence, the FE modeling for the cubic phantom was performed assuming a 2D plane-stress state. While this may be a fair assumption for ultrasound phantoms with simple geometries, realistic tissues are heterogeneous and out-of-plane motion may not be negligible. However, 3D ultrasound imaging is available [32], and progress has been made towards the estimation of 3D displacement and strain fields from ultrasound data [33]. Our method can be adapted for application to 3D strain images, since (4) is also available for elastic modulus estimation in 3D [27].

We used strain data rather than displacement data for the reconstruction of the elastic modulus distribution in the phantoms. Since strain is the spatial derivative of displacement, noise is amplified in the strain images compared to the displacement images. The use of a least-squares strain estimator [26], [29], rather than spatial differentiation, partially solved this problem. Back calculation of the elastic properties from displacement data is also possible and involves iterative optimization [34], [35]. Although believed to be more accurate, computation time is significantly increased for this method. Additionally, the compressions applied in the experiments were large, ranging from nearly 8% in the breast phantom experiment to 15% in the tests with the cubic phantom. Nonlinear material effects could have emerged at this range of strain in the gelatin-agar phantoms. As we applied a linear material model in the FE simulations, this could have introduced errors in the displacement predictions. Another source of errors could have been the registration of FE-predicted displacements to the ultrasound-measured displacement fields. In the current study, we have manually aligned the ultrasound-based displacement images to the FE model, using the inclusions as markers. In future, application of semi-automatic image registration methods in conjunction with our FE prediction technique should be investigated. Finally, sensitivity analyses with contact boundary conditions showed that incorporation of nonlinear boundary conditions could reduce the error between FE prediction and ultrasound measurement. The frictional coefficient lies in the range 0.0 to 1.0 and, since we lubricated the surface of the phantom, we expected that a value closer to 0.0 was more appropriate. Using frictional contact with $\mu = 0.1$ appeared to improve the FE predictions, indicating that friction plays a role. As this friction coefficient was chosen somewhat arbitrarily, this parameter should be validated with additional experiments in future studies.

The next step is to extend the methodology for prediction of target motion when surgical tools, such as needles for breast biopsies, are inserted into soft tissue. This requires experiments to measure the needle-tissue interaction forces, and synchronize the data with ultrasound images of the needle and target. This information will be used to generate FE models to describe the needle and target dynamics. In addition, dynamic target displacements may be strain-rate dependent, and therefore may require a viscoelastic material model. Recent work has shown the feasibility of estimating viscoelastic properties using dynamic ultrasound elastography [36]. Tissue rupture during needle insertion will also have to be simulated using techniques such as cohesive zone models, element deletion, or the extended FE method [37].

B. Conclusion

This paper demonstrates the feasibility of combining ultrasound elastography and FE modeling for predicting target motion under different loading and boundary conditions. The efficacy of this method was demonstrated using experiments on phantoms with both simple and realistic, organ-shaped geometries. The results showed the importance of modeling the organ geometry and boundary conditions for predicting target displacements, while a relative distribution of isotropic linear Young's modulus seems sufficient for accurate predictions. We envision using this technique for developing preoperative planning models for minimally invasive surgical interventions.

Acknowledgment

The authors thank Dr. Laurent Warnet and Ulrich Sachs for help with dynamic mechanical analysis, and Youri van Veen and Gerben te Riet o/g Scholten for help with phantom mold manufacturing.

References

[1] W. K. Hung, M. Ying, C. M. Chan, H. S. Lam, and K. L. Mak, "Minimally invasive technology in the management of breast disease," *Breast Cancer*, vol. 16, no. 1, pp. 23–29, 2009.

[2] G. Koukourakis, N. Kelekis, V. Armonis, and V. Kouloulias, "Brachytherapy for prostate cancer: a systematic review," *Adv. Urol.*, vol. 2009, no. 1, pp. 1–11, 2009.

[3] W. A. Kaiser, S. O. R. Pfleiderer, and P. A. T. Baltzer, "MRI-guided interventions of the breast," *J. Magn. Reson. Imag.*, vol. 27, no. 2, pp. 347–355, 2008.

[4] G. Schueller, C. Schueller-Weidekamm, and T. H. Helbich, "Accuracy of ultrasound-guided, large-core needle breast biopsy," *Eur. Radiol.*, vol. 18, no. 9, pp. 1761–1773, 2008.

[5] R. G. Stock and N. N. Stone, "Current topics in the treatment of prostate cancer with low-dose-rate brachytherapy," *Urologic Clin. North Amer.*, vol. 37, no. 1, pp. 83–96, 2010.

[6] N. Abolhassani, R. Patel, and M. Moallem, "Needle insertion into soft tissue: a survey," *Med. Eng. Phys.*, vol. 29, no. 4, pp. 413–431, 2007.

[7] E. E. Deurloo, K. G. Gilhuijs, L. J. Schultze Kool, and S. H. Muller, "Displacement of breast tissue and needle deviations during stereotactic procedures," *Investigative Radiol.*, vol. 36, no. 6, pp. 347–353, 2001.

[8] X. Chai, M. van Herk, J. B. van de Kamer, M. C. Hulshof, P. Remeijer, H. T. Lotz, and A. Bel, "Finite element based bladder modeling for image-guided radiotherapy of bladder cancer," *Med. Phys.*, vol. 38, no. 1, pp. 142–150, 2011.

[9] T. C. Shih, J. H. Chen, D. Liu, K. Nie, L. Sun, M. Lin, D. Chang, O. Nalcioglu, and M. Y. Su, "Computational simulation of breast compression based on segmented breast and fibroglandular tissues on magnetic resonance images," *Phys. Med. Biol.*, vol. 55, no. 14, pp. 4153–4168, 2010.

[10] G. Fichtinger, J. Fiene, C. W. Kennedy, G. Kronreif, I. I. Iordachita, D. Y. Song, E. C. Burdette, and P. Kazanzides, "Robotic assistance for ultrasound guided prostate brachytherapy," in *Proc. Med. Image Comput. Comput.-Assist. Intervent. (MICCAI) Conf.*, vol. 4791, no. 1, Brisbane, Australia, Oct.–Nov. 2007, pp. 119–127.

[11] H. Xu, A. Lasso, S. Vikal, P. Guion, A. Krieger, A. Kaushal, L. L. Whitcomb, and G. Fichtinger, "MRI-guided robotic prostate biopsy: A clinical accuracy validation," in *Proc.Med. Image Comput. Comput.-Assist. Intervent. (MICCAI) Conf.*, vol. 6363, no. 3, Beijing, China, Sep. 2010, pp. 383–391.

[12] S. P. DiMaio and S. E. Salcudean, "Interactive simulation of needle insertion models," *IEEE Trans. Biomed. Eng.*, vol. 52, no. 7, pp. 1167–1179, 2005.

[13] S. Misra, K. J. Macura, K. T. Ramesh, and A. M. Okamura, "The importance of organ geometry and boundary constraints for planning of medical interventions," *Med. Eng. Phys.*, vol. 31, no. 2, pp. 195–206, 2009.

[14] S. Misra, K. T. Ramesh, and A. M. Okamura, "Modeling of tool-tissue interactions for computer-based surgical simulation: A literature review," *Presence: Teleoperators and Virtual Enviornments*, vol. 17, no. 5, pp. 463–491, 2008.

[15] C. Tanner, J. A. Schnabel, D. Hill, D. J. Hawkes, M. O. Leach, and D. R. Hose, "Factors influencing the accuracy of biomechanical breast models," *Med. Phys.*, vol. 33, no. 6, pp. 142–150, 2006.

[16] O. Goksel, S. E. Salcudean, S. P. DiMaio, R. Rohling, and J. Morris, "3D needle-tissue interaction simulation for prostate brachytherapy," in *Proc.Med. Image Comput. Comput.-Assist. Intervent. (MICCAI) Conf.*, vol. 3749, no. 1, Palm Springs, USA, Nov. 2005, pp. 827–834.

[17] E. Dehghan, X. Wen, R. Zahiri-Azar, M. Marchal, and S. E. Salcudean, "Modeling of needle-tissue interaction using ultrasound-based motion estimation," in *Proc. Med. Image Comput. Comput.-Assist. Intervent. (MICCAI) Conf.*, vol. 4791, no. 1, Brisbane, Australia, Oct.–Nov. 2007, pp. 709–716.

[18] R. Alterovitz, K. Y. Goldberg, J. Pouliot, and I.-C. J. Hsu, "Sensorless motion planning for medical needle insertion in deformable tissues," *IEEE Trans. Info. Tech. Biomed.*, vol. 13, no. 2, pp. 217–225, 2009.

[19] J. Ophir, I. Céspedes, H. Ponnekanti, Y. Yazdi, and X. Li, "Elastography: A quantitative method for imaging the elasticity of biological tissues," *Ultrasonic Imaging*, vol. 13, no. 2, pp. 111–134, 1991.

[20] C. L. de Korte, E. I. Ignacio Céspedes, A. F. van Der Steen, and C. T. Lancée, "Intravascular elasticity imaging using ultrasound: Feasibility studies in phantoms," *Ultrasound in Med. Biol.*, vol. 23, no. 5, pp. 735–746, 1997.

[21] R. G. P. Lopata, M. M. Nillesen, H. H. G. Hansen, I. H. Gerrits, J. M. Thijssen, and C. L. de Korte, "Performance evaluation of methods for two-dimensional displacement and strain estimation using ultrasound radio frequency data," *Ultrasound Med. Biol.*, vol. 35, no. 5, pp. 796–812, 2009.

[22] F. Kallel and M. Bertrand, "Tissue elasticity reconstruction using linear perturbation method," *IEEE Trans. Med. Imag.*, vol. 15, no. 3, pp. 299–313, 1996.

[23] W. Khaled, S. Reichling, O. T. Bruhns, and H. Ermert, "ltrasonic strain imaging and reconstructive elastography for biological tissue," *Ultrasonics*, vol. 44, pp. e199–e202, 2006.

[24] D. T. Ginat, S. V. Destounis, R. G. Barr, B. Castaneda, J. G. Strang, and D. J. Rubens, "US elastography of breast and prostate lesions," *Radiographics*, vol. 29, no. 7, pp. 2007–2016, 2009.

[25] C. L. de Korte, E. I. Céspedes, A. F. van Der Steen, B. Norder, and K. te Nijenhuis, "Elastic and acoustic properties of vessel mimicking material for elasticity imaging," *Ultrasonic Imaging*, vol. 19, no. 2, pp. 112–126, 1997.

[26] R. G. P. Lopata, H. H. G. Hansen, M. M. Nillesen, J. M. Thijssen, and C. L. de Korte, "Comparison of one-dimensional and two-dimensional least-squares strain estimators for phased array displacement data," *Ultrasonic Imaging*, vol. 31, no. 1, pp. 1–16, 2009.

[27] M. Yamakawa and T. Shiina, "Tissue elasticity reconstruction based on 3-dimensional finite-element model," *Jpn. J. Appl. Phys*, vol. 38, no. 5B, pp. 3393–3398, 1999.

[28] J. Sciarretta, A. Samani, J. Bishop, and D. B. Plewes, "MR validation of soft tissue mimicing phantom deformation as modeled by nonlinear finite element analysis," *Med. Phys.*, vol. 29, no. 1, pp. 65–72, 2002.

[29] F. Kallel and J. Ophir, "A least-squares strain estimator for elastography," *Ultrasonic Imaging*, vol. 19, no. 3, pp. 195–208, 1997.

[30] T. J. Hall, A. A. Oberai, P. E. Barbone, A. M. Sommer, N. H. Gokhale, S. Goenezent, and J. Jiang, "Elastic nonlinearity imaging," in *Proc. Annu. Int. Conf. IEEE Eng. Med. Biol. Soc. (EMBC)*, Minneapolis, USA, Sep. 2009, pp. 1967–1970.

[31] T. R. Kumm and M. M. Szabunio, "Elastography for the characterization of breast lesions: Initial clinical experience," *Cancer Control*, vol. 17, no. 3, pp. 156–161, 2010.

[32] M. M. Nillesen, R. G. P. Lopata, H. J. Huisman, J. M. Thijssen, L. Kapusta, and C. L. de Korte, "3D Cardiac segmentation using temporal correlation of radio frequency ultrasound data," in *Proc. Med. Image Comput. Comput.-Assist. Intervent. (MICCAI) Conf.*, vol. 5762, no. 2, London, U.K., Sep. 2009, pp. 927–934.

[33] M. S. Richards, P. E. Barbone, and A. A. Oberai, "Quantitative three-dimensional elasticity imaging from quasi-static deformation: A phantom study," *Phys. Med. Biol.*, vol. 54, no. 3, pp. 757–779, 2009.

[34] M. M. Doyley, P. M. Meaney, and J. C. Bamber, "Evaluation of an iterative reconstruction method for quantitative elastography," *Phys. Med. Biol.*, vol. 45, no. 6, pp. 1521–1540, 2000.

[35] A. A. Oberai, N. H. Gokhale, and G. R. Feijóo, "Solution of inverse problems in elasticity imaging using the adjoint method," *Inverse Problems*, vol. 19, no. 2, pp. 297–313, 2003.

[36] C. Schmitt, A. Hadj Henni, and G. Cloutier, "Ultrasound dynamic micro-elastography applied to the viscoelastic characterization of soft tissues and arterial walls," *Ultrasound Med. Biol.*, vol. 36, no. 9, pp. 1492–1503, 2010.

[37] J.-H. Song, H. Wang, and T. Belytschko, "A comparative study on finite element methods for dynamic fracture," *Comput. Mechan.*, vol. 42, no. 2, pp. 239–250, 2007.

Jorn op den Buijs received the M.Sc. degree from Eindhoven University of Technology, The Netherlands, in 2003, and the Ph.D. degree from Mayo Clinic College of Medicine, in Rochester, Minnesota, in 2009, both in biomedical engineering. His doctoral research was on X-ray imaging and numerical simulation of solute transport in porous scaffolds for tissue engineering.

He then worked within the Division of Engineering of Mayo Clinic on the development of subject-specific biomechanical models for femur fracture risk prediction in the elderly. In 2010, he joined the Control Engineering group of the University of Twente, The Netherlands, as a post-doctoral fellow and is affiliated with MIRA - Institute of Biomedical Technology and Technical Medicine.

Hendrik H G Hansen (S'11) was born in Roermond, The Netherlands, in 1982. He received the M.Sc. degree in applied physics from the Eindhoven Univesity of Technology, The Netherlands, in 2000. Currently, he is pursuing the Ph.D. degree at the Clinical Physics Laboratory of the Radboud University Nijmegen Medical Centre, Nijmegen, The Netherlands.

The research project he is working on, focuses on noninvasive ultrasound strain imaging of carotid arteries. His current research interests include strain imaging, elastography, ultrasound, and atherosclerosis.

Richard G P Lopata (S'05–M'11) was born in 1980, in Oosterhout, The Netherlands. He received the M.Sc. degree in biomedical engineering from Eindhoven University of Technology, Eindhoven, The Netherlands, in 2004, after defending his Master's thesis on "Dynamic Contrast-Enhanced MR Imaging and Pharmacokinetic Modeling of Tumor Perfusion". Part of this research was performed at the MRI Institute and Wayne State University in Detroit MI, USA. In 2010, he received the Ph.D. degree after defending his dissertation titled "2D and 3D Strain Imaging: Methods and *In Vivo* Applications" at the Clinical Physics Lab of the Radboud University Nijmegen Medical Centre.

He has (co-)authored more than 15 peer-reviewed papers and won the Student Paper Award during the IEEE Ultrasonics Symposium (2006), as well as the EUROSON Young Investigator Award of the European Federation of Societies for Ultrasound in Medicine and Biology (2008). Recently, he won the Best Student Oral Presentation Award at both the Dutch Biomedical Engineering Meeting and the International Tissue Elasticity Conference (2009). Currently, he is employed as a post-doc at Eindhoven University of Technology, Eindhoven, The Netherlands, and the University of Maastricht, Maastricht, The Netherlands, developing new screening techniques of abdominal aortic aneurysms. His research interests include primarily strain imaging, elastography, 2D and 3D ultrasound, muscle dynamics, and heart disease. Other areas of interest are MRI, signal processing, biological modeling, and identifiability analysis.

Chris L de Korte (M'01) born in 1969, received the M.Sc. Degree in medical electrical engineering from Eindhoven University of Technology, Eindhoven, The Netherlands, in 1993. The practical work was performed at the Biophysics Laboratory, Institute of Ophthalmology, University Hospital Nijmegen, The Netherlands, from 1992 to 1993. He studied the acoustical properties of eye tissues. In 1999, he received the Ph.D. degree in medical sciences at the Thoraxcenter, Erasmus University Rotterdam, The Netherlands, on the subject "Intravascular Ultrasound Elastography."

From 1999 to 2002, he was Principal Investigator of the project to translate intravascular palpography to clinical applications. In 2002, he joined the Clinical Physics Laboratory of the Radboud University Nijmegen Medical Center in Nijmegen, The Netherlands, as Assistant Professor. In 2004, he became Head of the laboratory, and from 2006 he is Associate Professor of medical ultrasound techniques. He has (co-)authored more than 80 peer-reviewed articles in international journals, is (co-)inventor of three patents, and is recipient of the EUROSON Young Investigator Award, 1998, of the European Federation of Societies for Ultrasound in Medicine and Biology. He organized the International Tissue Elasticity Conference, in 2009. His main research interests are functional imaging using ultrasound, acoustical and mechanical tissue characterization, and ultrasound image segmentation for cardiac, vascular, muscular, and other applications.

Sarthak Misra (S'05 - M'10) received his Master's degree in Mechanical Engineering from McGill University, Montreal, Canada. He received the Ph.D. degree in mechanical engineering from the Johns Hopkins University, Baltimore, USA.

Prior to commencing his studies at Johns Hopkins, he worked for three years as a Dynamics and Controls Analyst on the International Space Station Program. He joined the University of Twente, Enschede, The Netherlands, as an Assistant Professor, in 2009. He is a member of the Control Engineering Group and is affiliated with MIRA - Institute for Biomedical Technology and Technical Medicine. His research interests are in biomechanics and robotics. He is the recipient of 2010 Netherlands Organization for Scientific Research (NWO) VENI Award. He is an Associate Editor of the IEEE Robotics and Automation Society (RAS) Conference Editorial Board.